Cholesterol inhibits HCN channels through dual mechanisms in neuropathic pain

Lucas J. Handlin[a], Clémence Gieré[b], Nicolas L.A. Dumaire[b], Lyuba Salih[b], Aubin Moutal[b], and Gucan Dai[a,1]

Author Affiliations

[a]Edward A. Doisy Department of Biochemistry and Molecular Biology, Saint Louis University School of Medicine

[b]Department of Pharmacology and Physiology, Saint Louis University School of Medicine

[1]Correspondence: Gucan Dai (email: gucan.dai@health.slu.edu)

ABSTRACT

Hyperpolarization-activated cyclic nucleotide-gated (HCN) channels regulate the excitability of dorsal root ganglion (DRG) neurons, particularly in the context of neuropathic pain. Cholesterol, a major component of lipid-ordered membrane domains (OMDs), has recently been identified as a critical modulator of HCN channel function. Using FLIM-FRET-based OMD probes and a fluorescent cholesterol sensor GRAM-W, we investigated the effects of cholesterol supplementation on nociceptor DRG neurons from a rat model of spared nerve injury (SNI). We developed a method to distinguish at least two phases of membrane remodeling during cholesterol enrichment: an initial phase marked by OMD expansion and increased accessible cholesterol, followed by a second phase with continued cholesterol accumulation without further OMD expansion. These cholesterol dynamics were further validated through changes in fluorescence anisotropy and homo-FRET measurements of GRAM-W. Temporal analysis of cholesterol enrichment revealed two mechanisms of HCN channel modulation: through expansion of OMDs and elevation of free cholesterol. In SNI DRG neurons with low cholesterol and small OMDs, both mechanisms are active, while in naïve DRG neurons—characterized by high cholesterol and large OMDs—modulation occurs only via increased free cholesterol. These findings deepen our understanding of cholesterol's role in modulating ion channels and contributing to neuropathic pain.

INTRODUCTION

Cholesterol-mediated modulation of ion channel function remains an area of intense investigation, with longstanding debates about whether its effects arise from direct molecular interactions or from alterations in membrane organization (1-4). Emerging evidence suggests that cholesterol-rich, lipid-ordered membrane domains—also known as ordered membrane domains (OMDs)—play a crucial role in organizing membrane proteins and signaling complexes, thereby influencing the functional properties of ion channels (4-8). Among these, hyperpolarization-activated cyclic nucleotide-gated (HCN) channels have emerged as key players in the pathophysiology of neuropathic pain (9-11). HCN channels regulate neuronal excitability through generating "I_h current", which is mostly sodium inward current in physiological conditions that can promote membrane depolarization (12-15). Aberrant upregulation or altered gating of HCN channels in sensory neurons has been linked to increased excitability and spontaneous firing, hallmarks of chronic pain states (9, 16, 17). Recent findings indicate that the function and voltage sensitivity of HCN channels are modulated by their localization within OMDs, suggesting a lipid-dependent mechanism of regulation (8). Disruption of OMDs dramatically alters native HCN currents, pointing to OMDs as key modulators of HCN channel activity in the context of neuropathic pain (8, 18). Understanding how cholesterol and OMDs regulate HCN channels could reveal novel therapeutic strategies for targeting pathological hyperexcitability in neuropathic pain.

Our study provides new evidence that cholesterol dynamically regulates HCN channel gating through a dual mechanism: by modifying OMDs and by altering free, accessible cholesterol levels in the inner leaflet of the plasma membrane. By integrating fluorescence lifetime imaging (FLIM-FRET), genetically encoded cholesterol sensors, and homo-FRET-based anisotropy imaging, we reveal a biphasic response to cholesterol enrichment at the plasma membrane: an initial OMD expansion phase within 5 minutes, followed by a sustained increase in inner and outer leaflet cholesterol. This distinction is useful, as it allows us to temporally separate the impact of OMDs from that of cholesterol accumulation, addressing a persistent challenge in membrane biophysics. Our findings have direct implications for neuropathic pain pathophysiology. In a nerve injury model, we show that DRG neurons exhibit smaller OMDs and reduced inner-leaflet cholesterol. In vivo, cholesterol depletion induced mechanical hypersensitivity in naïve rats while cholesterol supplementation alleviated mechanical hypersensitivity in a model of chronic neuropathic pain. These changes correlate with altered HCN channel gating, providing a mechanistic link between lipid remodeling and hyperexcitability in chronic pain states. By elucidating how cholesterol dynamically regulates HCN channels, this study opens new avenues for investigating cholesterol-mediated modulation of ion channels in excitable cells.

RESULTS

Temporally separating the effect of cholesterol enrichment on plasma membrane properties

To define how cholesterol modulates membrane excitability, we first examined changes in plasma membrane properties following cholesterol enrichment. Because cholesterol is an inherent component of OMDs, distinguishing its specific effects from those of OMDs on membrane proteins remains challenging. Altering one without affecting the other was not feasible. To understand the roles of cholesterol itself versus the OMDs, in combination of the OMD probes, we used a genetically encoded cholesterol sensor eGFP-GRAM-W that labels the inner leaflet accessible cholesterols (19) (Fig. 1A and Supplementary Fig. 1). The GRAM-W sensor is derived from the GRAM (Glucosyltransferases, Rab-like GTPase Activators, and Myotubularins) cholesterol-binding domain of the cholesterol transport protein $GRAMD_{1b}$, with a glycine mutated to tryptophan (G187W) (19-21). This mutation enhances its localization to the plasma membrane. Compared to traditional cholesterol sensors, such as those derived from perfringolysin O (PFO-D4) or anthrolysin O (ALO-D4), which often bind to cytosolic cholesterol, GRAM-W offers improved plasma membrane targeting and specificity (19). This makes GRAM-W a more reliable tool for studying cholesterol dynamics at the plasma membrane. In addition, a mCherry-tagged ostreolysin A (OlyA) was used to report levels of outer leaflet cholesterol/sphingomyelin (SM) complexes (22, 23) (Fig. 1A). Cholesterols sequestered by SM cannot be probed by conventional cholesterol sensors like PFO-D4 (24). In addition, we used the previously established FRET-based OMD probes as reporters of the OMD size, using cholera toxin subunit B (CTxB)-conjugated (8) or peptide (L10)-based FRET pairs (25-28).

Applying these four probes individually and overlaying their time courses following WSC treatment in tsA-201 cells revealed a biphasic effect of cholesterol enrichment on plasma membrane properties. Within the first 5 minutes, we observed an increase in FRET between CTxB-Alexa Fluor 488 (AF-488)/Alexa Fluor 647 (AF-647) and a decrease in FRET between L10-CFP/L10-YFP. For the AF-488/AF-647 pair, the FRET efficiency increased from 9% to 11.8% ($p = 0.02$), while for the L10 FRET pair, the FRET efficiency decreased from 7.6% to 3.3% ($p = 0.039$). As previously demonstrated, these opposing FRET changes both indicate OMD expansion (8) (Fig. 1B). The FRET changes plateaued within 5 minutes. In contrast, GRAM-W and OlyA fluorescence at the plasma membrane continued to increase beyond the first 5 minutes, extending throughout the 15-20-minute timeframe (19). These results suggest that the initial phase (lasting no more than 5 minutes) involves OMD expansion along with increases in inner leaflet cholesterol and outer leaflet cholesterol/SM complexes. The second phase primarily reflects a continued accumulation of cholesterol, either in free form or bound to SM, in tsA-201 cells. This finding

provides an experimental strategy to temporally distinguish the effects of OMD expansion from cholesterol itself on ion channel gating in DRG neurons.

We applied the same strategy to evaluate the effects of WSC supplementation on small-diameter nociceptor DRG neurons from both naïve rats and rats subjected to the spared nerve injury (SNI) model of neuropathic pain (29). As we previously demonstrated, nociceptor DRG neurons in the SNI model exhibit significantly smaller OMDs compared to the large OMDs observed in naïve nociceptor DRG neurons (8). In both conditions, membrane-localized fluorescence intensity of the GRAM-W sensor showed a sustained increase over the 15-minute WSC treatment (Fig. 1 C and D). However, the CTxB-based FRET reporter of OMD size exhibited minimal changes in FLIM-FRET efficiency for naïve DRG neurons, whereas SNI DRG neurons showed a substantial increase within 5 minutes (Fig. 1 C and D). The initial FLIM-FRET efficiency measured using CTxB-based probes was significantly lower in SNI DRG neurons (6.3%) than in naïve neurons (17.3%) and slightly lower than in tsA-201 cells (9%). Notably, following WSC supplementation, the OMD changes detected by CTxB-based FRET in SNI DRG neurons closely mirrored those observed in tsA-201 cells, reaching an increase of 12.7%.

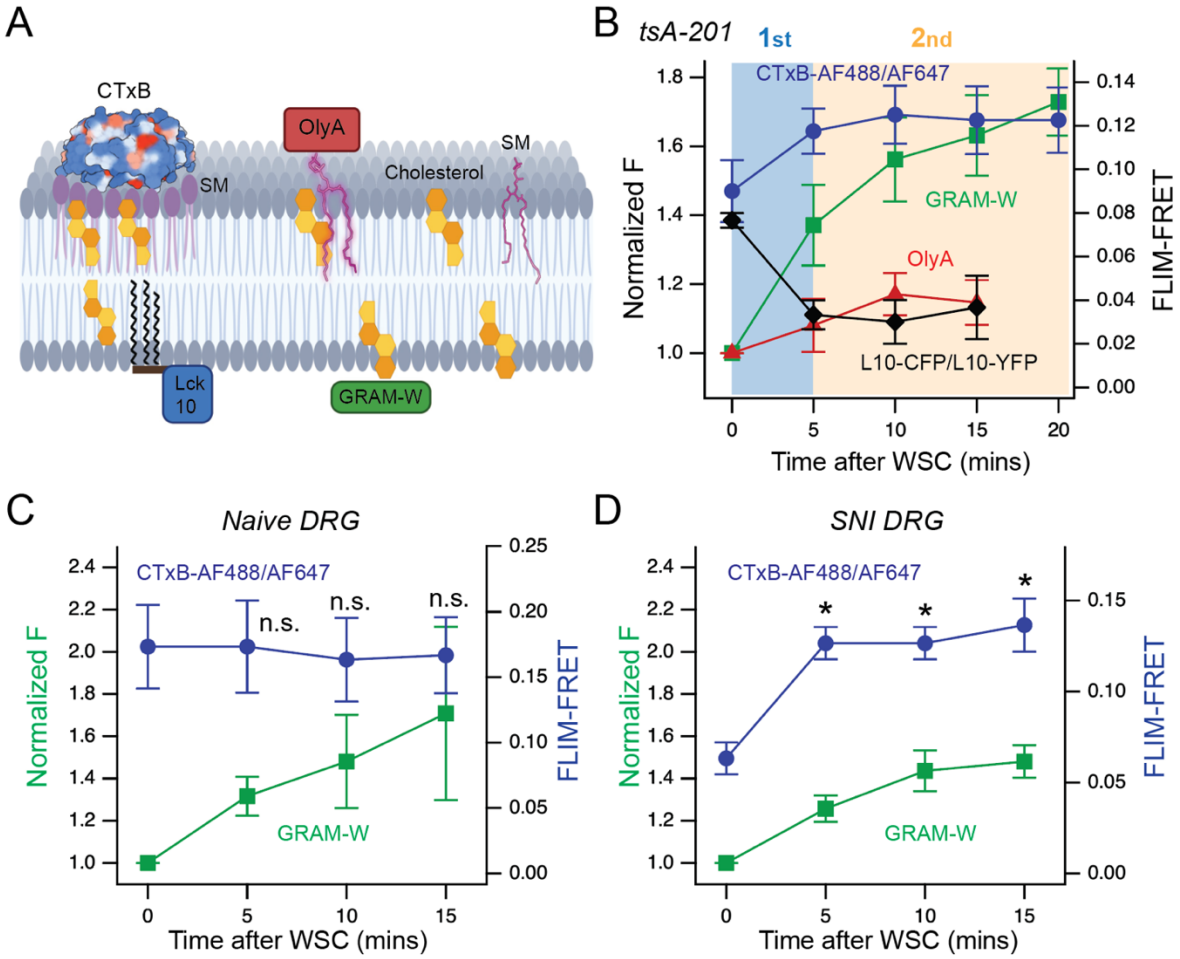

Fig. 1. Modulation of plasma membrane (PM) properties by cholesterol enrichment.
(**A**) Strategies implemented to report the plasma membrane properties after WSC-mediated cholesterol supplementation. A mCherry-labeled ostreolysin A (OlyA) was used to recognize outer leaflet cholesterol/SM complexes, whereas GRAW-W-eGFP was used to label free cholesterol levels in the inner leaflet of the PM. The OMD size at the PM was probed using FRET-based reporters, either cholera toxin subunit B (CTxB)-conjugated or peptide (L10)-based FRET pairs. (**B**) Time course of the change in normalized fluorescence intensity at the PM or the FLIM-FRET efficiency post 0.5 mg/mL WSC application for tsA201 cells. Data shown are mean + s.e.m., n = 3 - 10 cells. (**C**-**D**) Summary time course of the change in normalized GRAM-W fluorescence intensity at the PM and the FLIM efficiency of CTxB-AF488/AF647 FRET post 0.5 mg/mL WSC application for naïve DRG neurons (C) and for nociceptor DRG neurons of the SNI model animals (D). Data shown are mean + s.e.m., n = 3 - 4 cells. The FRET levels of CTxB pairs showed a significant increase after WSC for SNI DRG neurons (*$p < 0.05$ using paired t-test) but no change for naïve neurons (n.s.: no statistical significance).

Homo-FRET based fluorescence anisotropy measurement of membrane cholesterol density.

Furthermore, we performed homo-FRET-based live-cell anisotropy for imaging membrane-localized GRAM-W fluorescence (Fig. 2 A-C). Fluorescence anisotropy measures the polarization of emitted light, enabling the quantification of homo-FRET by detecting depolarization resulting from energy transfer between nearby fluorophores. A decrease in anisotropy reflects increased homo-FRET efficiency, indicating closer proximity or clustering between the probes (30). Homo-FRET-based anisotropy is sensitive to the organization and density of fluorophores while being less influenced by factors such as photobleaching of fluorophores (31). This sensitivity enables a more accurate quantification of inner-leaflet cholesterol density, which would be challenging to resolve using intensity-based fluorescence alone. Following WSC supplementation, we observed a continued decrease in GRAM-W fluorescence anisotropy, accompanied by an increase in homo-FRET efficiency (Fig. 2 A-C). Notably, the initial homo-FRET efficiency was highest in naïve DRG neurons but lower in tsA-201 cells and DRG neurons of the SNI model. These results suggest that free, accessible cholesterol in the inner leaflet is also reduced after nerve injury, representing a novel finding in addition to the previously reported decrease in OMD size in neuropathic pain (8).

We also performed anisotropy experiments using OlyA-mCherry and observed distinct differences in homo-FRET responses to WSC treatment across tsA-201 cells, naïve DRG neurons, and SNI DRG neurons (Fig. 2 D-F). In tsA cells, anisotropy and homo-FRET revealed small but significant changes, aligning with the modest increase in outer leaflet cholesterol/SM complexes as concluded from the intensity-based measurements. In naïve DRG neurons, anisotropy and homo-FRET values remained unchanged after WSC treatment, in contrast to the noticeable decrease in anisotropy and corresponding increase in homo-FRET observed in SNI DRG neurons. Notably, baseline homo-FRET values were highest in naïve DRG neurons and reduced in SNI DRG neurons, consistent with a decrease in OMD size following nerve injury. Given that OlyA binds to cholesterol/SM complexes enriched in OMDs, the

high baseline homo-FRET and lack of response to cholesterol supplementation in naïve DRG neurons suggest that these cells likely already contain saturated levels of cholesterol/SM complexes that cannot be further increased by adding free cholesterol. This implies that the availability of sphingomyelin, rather than cholesterol, may be the limiting factor.

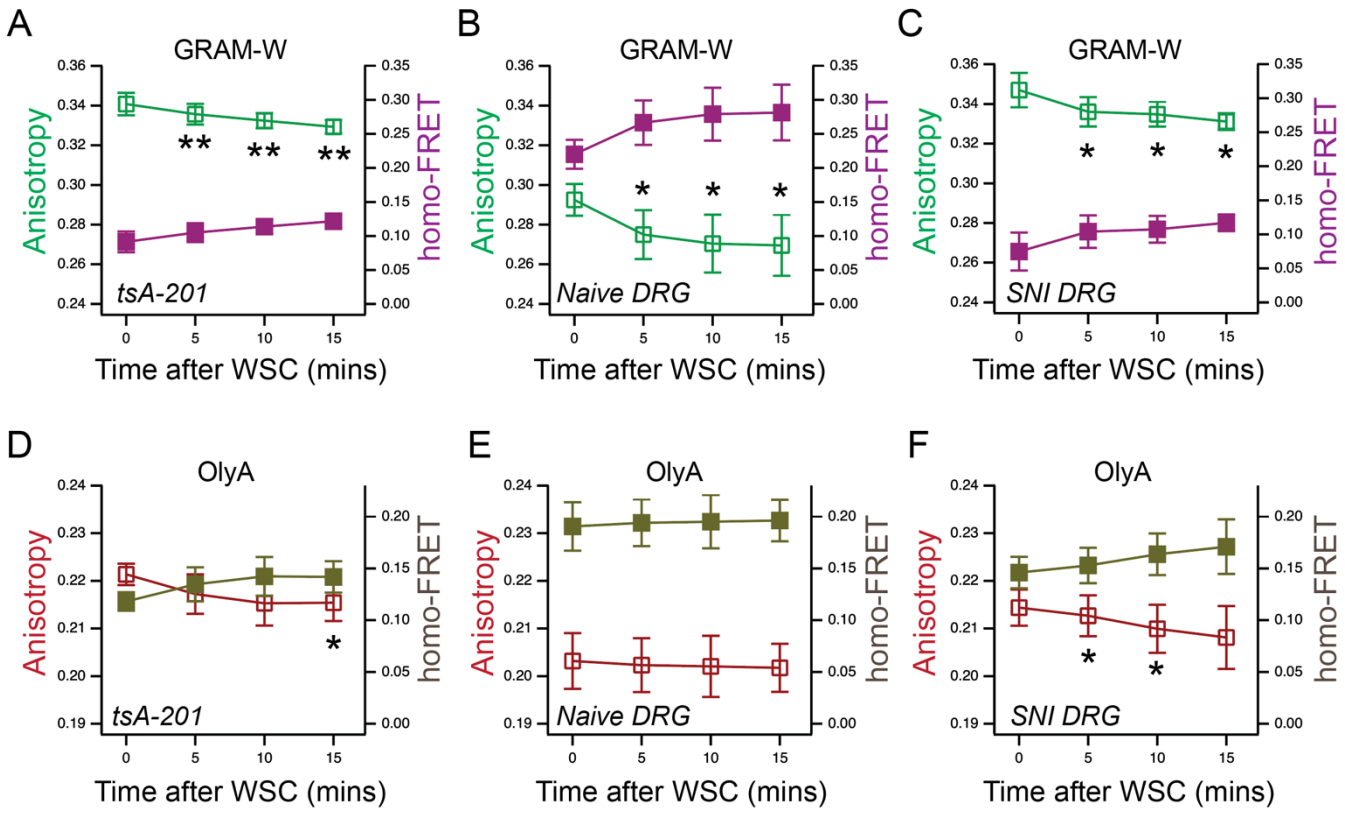

Fig. 2. Fluorescence anisotropy reports homo-FRET between cholesterol sensors.
(**A-C**) Summary time course of the changes in GRAM-W fluorescence anisotropy and estimated homo-FRET efficiency for tsA cells (A, n = 10), naïve DRG neurons (B, n = 4), and DRG neurons of SNI model animals (C, n = 4). (**D-F**) Summary time course of the changes in GRAM-W fluorescence anisotropy and estimated homo-FRET efficiency for tsA cells (D, n = 4), naïve DRG neurons (E, n = 5), and DRG neurons of SNI model animals (F, n = 3). Data shown are mean + s.e.m., *p < 0.05, **p < 0.01 using paired t-test.

Bidirectional modulation of the HCN channel gating by cholesterol in nociceptor DRG neurons

Previously, we modulated cholesterol levels in DRG neurons for electrophysiological measurements using methyl-β-cyclodextrin (mβCD) for extraction or water-soluble cholesterol (WSC) for supplementation, achieved by preloaded methyl-β-CD-cholesterol complexes (8, 32, 33). These treatments were brief (30 sec to 1 min) and applied prior to whole-cell patch-clamp recordings on separate control and treated cells. Here, we applied these reagents directly to the same patch during whole-cell recordings and compared hyperpolarization-activated HCN currents in nociceptor DRG neurons before

and after more prolonged treatments (Fig. 3). We found that 0.5 mg/mL WSC supplementation significantly inhibited HCN current, reducing the amplitude of currents elicited by a maximal hyperpolarizing voltage, suggesting a decrease in channel open probability, and shifting the half-maximal activation voltage leftward for the conductance-voltage (G-V) relationship ($\Delta V_{1/2}$ = 8.4 mV after 10 mins of WSC treatment) (Fig. 3 D and E). These effects on the G-V relationship and current amplitude persisted in the presence of additional cAMP at a supersaturating concentration of 0.5 mM in the pipette solution, with a $\Delta V_{1/2}$ of ~ 6 mV and a ~25% reduction in current amplitude following 10 minutes of WSC treatment. In contrast, cholesterol extraction (5 mM mβCD) produced nearly opposite effects, increasing current amplitude (Fig. 3C and Supplementary Fig. 2), though it had minimal impact on $V_{1/2}$, with or without the additional 0.5 mM cAMP (8). Instead, cholesterol extraction increased the slope factor (V_s) of the G-V relationship (8), whereas WSC treatment caused only a negligible change in V_s for naïve nociceptor neurons either with or without the additional 0.5 mM cAMP (Fig. 3F). Since the V_s reflects voltage sensor movement and is influenced by the OMD localization of HCN channels, it may serve as a reporter of OMD dimensions of DRG neurons (8, 27). We propose that these effects arise from the naturally high cholesterol content and large OMDs in naïve DRG neurons. In this context, further increases in cholesterol levels may primarily elevate free accessible cholesterol, leading to a shift in $V_{1/2}$ and a decrease in open probability without affecting the V_s. Our findings lead to a model in which cholesterol modulates HCN channels through a dual mechanism: by altering OMD size and potentially interacting directly with the channels at the inner leaflet of the membrane. Moreover, this substantial modulation of HCN current amplitude (and open probability) is physiologically significant and was validated through the same patch-clamp experiments. Compared to changes in the slope factor, alterations in current amplitude may have a greater impact on action potential firing and may contribute more directly to neuronal excitability.

Beyond the equilibrium parameters of HCN gating, we found that the activation kinetics of HCN channels in nociceptor DRG neurons were modulated by cholesterol in the same patch-clamp experiments. The most prominent effect was a significant acceleration of channel activation following treatment with 5 mM mβCD, which shortened the primary activation time constant (τ_1) from an average of 80 ± 4.3 ms to 52 ± 2.9 ms, at the saturating hyperpolarizing voltage of –140 mV (Fig. 4A). This effect was also present at other hyperpolarizing voltages (Fig. 4B). In contrast, cholesterol enrichment with 0.5 mg/mL WSC for 5 mins slowed channel activation, increasing τ_1 from an average of 72 ± 9.6 ms to 88 ± 8.7 ms at –140 mV, although this effect was less pronounced than that of mβCD (Fig. 4 C and D). The mβCD-induced acceleration of activation persisted in the presence of 0.5 mM cAMP in the pipette solution (Supplementary Fig. 2). However, under the same cAMP conditions, effect of WSC treatment on τ_1 was

no longer significant (τ_1 from an average of 55 ± 3.5 ms to 52.3 ± 5.5 ms), likely because the cAMP potentiation of channel activation is predominant. Together, these findings suggest that HCN channel activation is highly sensitive to cholesterol levels. In addition, our recent findings on cholesterol-mediated modulation of current amplitude and activation kinetics (8) were further substantiated in this study, offering new insights into the mechanisms by which HCN channels influence neuronal excitability.

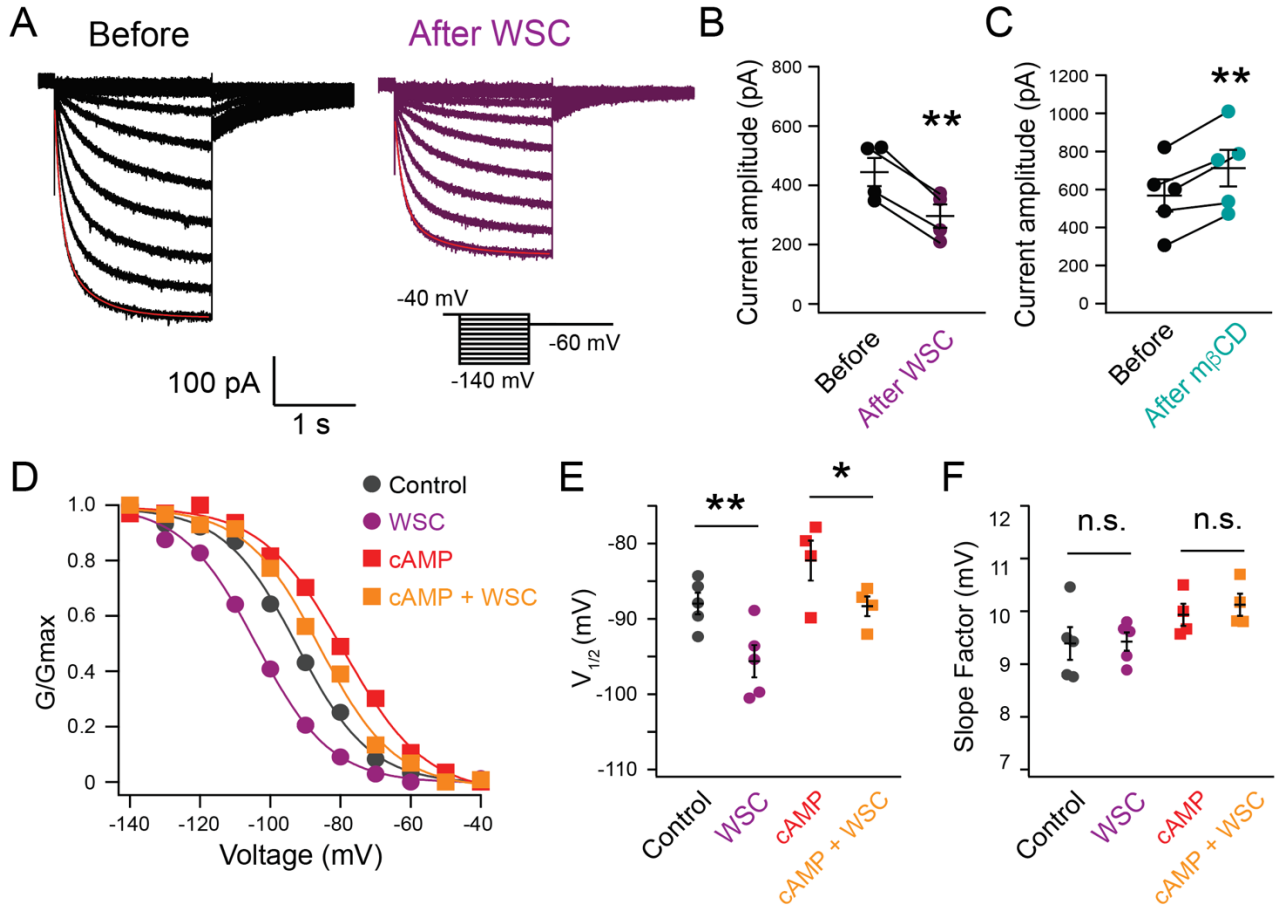

Fig. 3. Effects of cholesterol manipulation on the equilibrium aspect of HCN channel gating in nociceptor DRG neurons.
(**A**) Application of WSC decreased the current amplitude of HCN currents in the same-patch experiment. Double-exponential fittings (in red) of the current traces at -140 mV are highlighted. (**B**) Amplitude of HCN currents elicited by a saturating hyperpolarizing voltage was used for the graph comparing the before and after treatments. Data shown are mean + s.e.m., n = 4 patches, **p < 0.01. Paired t-test were used. (**C**) Effects of the acute mβCD treatment on current amplitude of HCN currents, recorded from the same patch, showing opposite directional change as in panel B. Data shown are mean + s.e.m., n = 5 patches, **p < 0.01. Paired t-test were used. (**D**) Representative G-V relationship of HCN channel activation recorded from same-patch experiments before and after 5 minutes of 0.5 mg/mL WSC application, in the presence or absence of 0.5 mM additional cAMP. (**E-F**) Summary of the parameters derived from Boltzmann fitting of the G-V relationship of HCN channel activation before and after the WSC treatment: $V_{1/2}$ in panel E and slope factors (V_s) in panel F, n.s.: no statistical significance. n = 5 cells without added cAMP and n = 4 with added 0.5 mM cAMP, *p < 0.05, **p < 0.01, paired t-test.

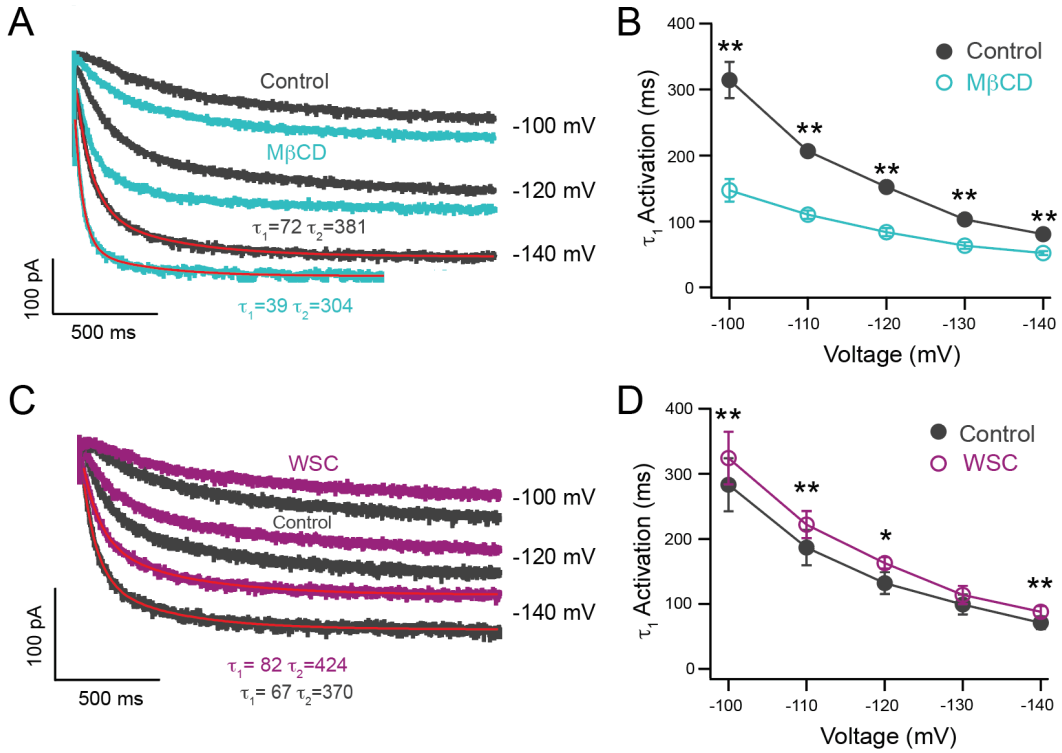

Fig. 4. Effects of cholesterol on the kinetics of HCN channel activation in nociceptor DRG neurons. (**A**, **C**) HCN channel currents elicited by different hyperpolarizing voltages were shown with double-exponential fits to highlight the acceleration of channel activation by mβCD (A) and the slowdown of channel activation by WSC (C). (**B**, **D**) Summary graph illustrating the effects of mβCD (B) and WSC (D) on the τ_1 of channel activation at different voltages. Data shown are mean + s.e.m., n = 6 - 7 cells, *p < 0.05, **p < 0.01, paired t-test.

Dissecting the dual effects of cholesterol supplementation on HCN channel gating

Based on our FLIM-FRET and anisotropy experiments indicating that the effects of cholesterol enrichment can be temporally teased apart using the 15-minute WSC supplementation protocol, we applied this approach to examine whether the cholesterol-mediated modulation of HCN channel gating could exhibit two phases. We conducted same-patch time-course experiments to quantify the effects of WSC (0.5 mg/mL) supplementation on HCN channel gating parameters by recording native HCN currents from both naïve DRG neurons and DRG neurons of the SNI model at 5-minute intervals (Fig. 5 A-C). Each HCN current-recording series required over two minutes to complete. In naïve DRG neurons, the slope factor V_s remained unchanged (Fig. 5A). In contrast, the $V_{1/2}$, current amplitude, and the primary activation time-constant τ_1 exhibited significant alterations throughout the ~15 minutes of WSC treatment, with the most pronounced effects observed within the first 5 minutes (Fig. 5A-C). Furthermore, DRG neurons from the SNI model displayed changes in all gating parameters over the course of WSC

exposure (Fig. 5 D-F). The change in the V_s occurred mostly within the first 5 minutes (Fig. 5D). Control experiments conducted without WSC treatment or additional 0.5 mM cAMP showed only modest changes, likely reflecting the gradual dilution of endogenous cytosolic cAMP ($\Delta V_{1/2}$ = ~ 4 mV after 10 minutes, Supplementary Fig. 3). The smaller shift in $V_{1/2}$ compared to that with WSC-treated neurons (Fig. 5) supports that the observed effects were specifically induced by WSC. These findings suggest that the reduction in the slope factor primarily reflects the expansion of OMDs, whereas the changes in $V_{1/2}$, current amplitude, and τ_1 for activation are predominantly driven by an increased accumulation of accessible cholesterols in the plasma membrane. Cholesterols could exert direct binding effects on HCN channels in DRG neurons, as suggested by a putative cholesterol binding site of HCN3 channels (34), which is conserved across all HCN isoforms.

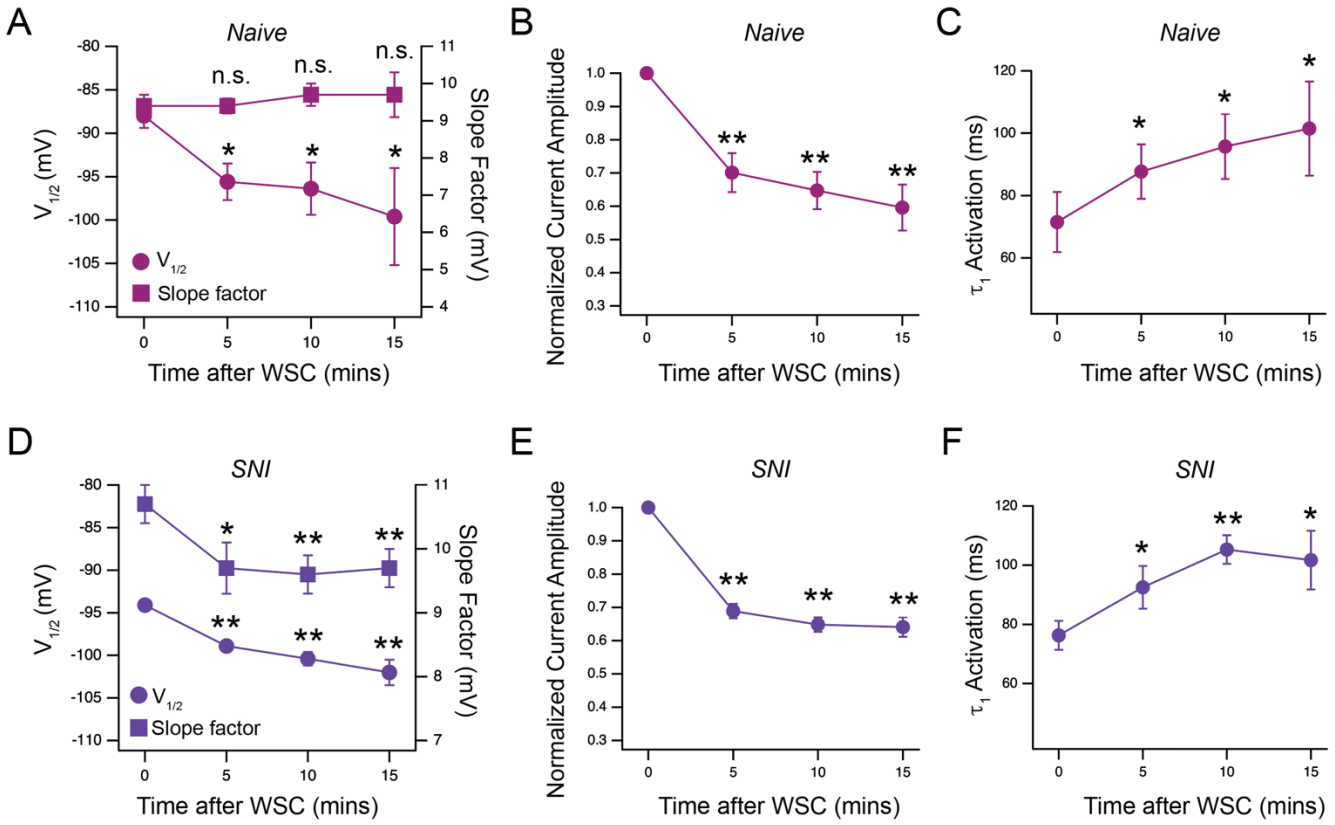

Fig. 5. Time course of the HCN channel modulation during cholesterol enrichment in nociceptor DRG neurons from naïve and SNI animals.
(**A-C**) Summary time course of the change in the $V_{1/2}$ and slope factor (V_s) (A), the current amplitude (B), and τ_1 of channel activation (C) after 0.5 mg/mL WSC application for naïve small DRG neurons, n.s.: no statistical significance. (**D-F**) Summary time course of the change in the $V_{1/2}$ and slope factor (V_s) (D), the current amplitude (E), and τ_1 of channel activation (F) after 0.5 mg/mL WSC application for SNI small DRG neurons. Data shown are mean + s.e.m., n = 4 - 7 cells, *p < 0.05, **p < 0.01, paired t-test.

We previously demonstrated that the voltage sensor S4 helix of the HCN channel is sensitive to changes in OMD size in DRG neurons (8, 27). Notably, the unusually long S4 segment in HCN channels (27, 35, 36) may underlie their unique susceptibility to dual modulation by cholesterol and OMDs, a feature not commonly observed in other voltage-gated ion channels. To assess whether this mechanism extends to other key ion channels involved in DRG neuron excitability, we recorded sodium currents from small nociceptive DRG neurons following cholesterol depletion (Supplementary Fig. 4). Particularly, sodium channels in DRG neurons play important roles in controlling action potential firing and pain sensation (37, 38). Similarly to previous findings (39, 40), mβCD treatment caused a slight hyperpolarizing shift in the activation curve ($\Delta V_{1/2}$ = ~ 5 mV), without affecting the slope factor of activation or steady-state parameters of the fast inactivation. In contrast, as we emphasize in this study, cholesterol depletion increases the slope factor of the G-V relationship for HCN channels in small DRG neurons, suggesting a decrease in the effective gating charge movement associated with channel activation (8). Sodium channels may not preferentially localize to OMDs, or their shorter S4 segments may lack sensitivity to changes in membrane domain organization (41). These findings suggest that the dual modulatory effect of cholesterol on HCN channels may represent a channel-specific mechanism not shared by voltage-gated sodium channels.

Cholesterol levels bidirectionally modulate mechanical pain sensitivity

To assess whether cholesterol manipulation could affect pain behaviors of rats in vivo, we tested if a local administration of cholesterol-depleting or cholesterol-supplementing agents in naïve or SNI neuropathic pain rats resulted in changes of mechanical hypersensitivity. Intraplantar injection of β-cyclodextrin (β-CD), but not its inactive analog α-cyclodextrin, induced significant mechanical hypersensitivity in naïve rats, as evidenced by a time-dependent reduction in paw withdrawal threshold on the injected paw compared to the contralateral control paw and α-cyclodextrin–injected animals (Fig. 6A). This effect persisted for 24 hours and was quantitatively confirmed (Fig. 6B), highlighting a clear pronociceptive effect of acute cholesterol chelation in naïve animals. We next examined whether cholesterol supplementation could alleviate established mechanical hypersensitivity in rats with spared nerve injury (SNI), a well-characterized model of neuropathic pain (42, 43). Intraplantar injection of water-soluble cholesterol (WSC) partially reversed mechanical hypersensitivity in the injured paw, while having no effect on the non-injured contralateral paw (Fig. 6 C and D). The anti-hypersensitivity effect was sustained for 4 hours. Together, these findings demonstrate that cholesterol homeostasis plays a critical role in regulating nociceptive thresholds under both physiological and neuropathic pain conditions. Cholesterol depletion enhances pain sensitivity, while cholesterol supplementation reverses mechanical hypersensitivity, supporting a model in which cholesterol acts as a dynamic modulator of pain signaling.

Moreover, these findings provide in vivo evidence supporting the therapeutic potential of cholesterol enrichment and are consistent with our observations in cultured nociceptor DRG neurons, where WSC treatment reduces neuronal hyperexcitability (8).

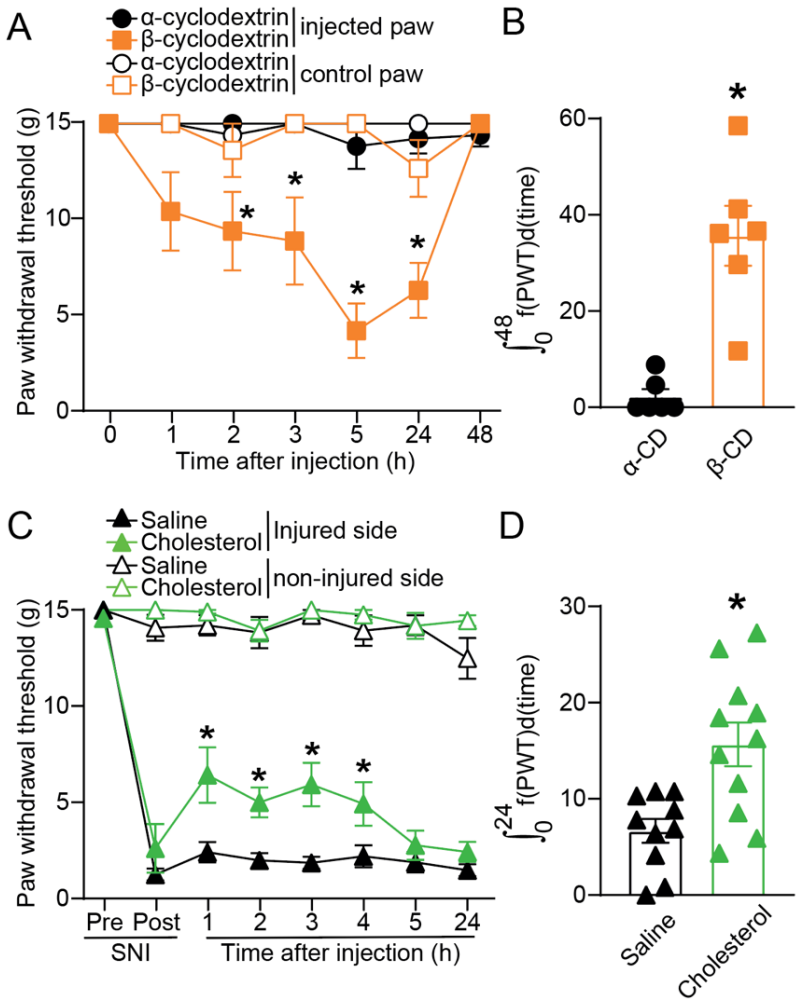

Fig. 6. Cholesterol regulates mechanical hypersensitivity in both naïve and neuropathic pain rats. (**A-B**) Naïve rats were injected intraplantarly with β-cyclodextrin (β-CD) or its ineffective analog, α-cyclodextrin (α-CD) (20 mM each in 50 µl), and paw withdrawal threshold was measured. (**A**) Graph showing the hind-paw withdrawal threshold of naïve rats injected as indicated. The threshold for the injected paw versus the uninjected paw for each group is shown. β-CD, but not α-CD, induced mechanical hypersensitivity in the injected paw compared to the control paw and α-CD-injected groups. (**B**) Bar graph with scatter plot showing the integrated area of the data in the panel A (from 0 to 48 h), demonstrating a significant reduction in PWT over time in the β-CD-injected paw group (n = 6 rats per group). (**C-D**) Rats received a spared nerve injury (SNI) and developed chronic neuropathic pain. Rats then received an intraplantar injection of WSC (50 µl). (**C**) Graph showing the paw withdrawal threshold of rats with SNI injected as indicated. For each rat, both the injured and non-injured paws were injected, and withdrawal thresholds were measured. WSC injection significantly reversed mechanical hypersensitivity on the injured side of SNI rats while having no effect on the control contralateral side. (**D**) Bar graph with scatter plot showing the integrated area of the data in panel C (from 0 to 24 h), demonstrating a significant anti-hypersensitivity effect of cholesterol compared to saline-treated SNI rats (n = 10 - 11 rats per group). Data are presented as mean ± SEM. *p < 0.05 compared to the control.

DISCUSSION

Our approach establishes a framework for investigating the effects of cholesterol on ion channels and membrane properties. By combining FLIM-FRET-based imaging of OMDs, cholesterol sensors, and homo-FRET-based anisotropy imaging, we have developed a strategy to temporally distinguish the contributions of OMDs from those of free, accessible cholesterol in the plasma membrane. This approach can be broadly applied to study other membrane proteins regulated by lipid microenvironments, such as voltage-gated potassium channels, G-protein-coupled receptors, and mechanosensitive ion channels. Many of these proteins localize to or interact with OMDs, yet their regulation by cholesterol remains poorly understood. By dissecting dynamic changes in compartmentalized nanodomains and cholesterol distribution, our methodology enables future studies to explore how cholesterol modulates ion channels and impinges on neuronal excitability.

In the context of neuropathic pain, upregulation of HCN channels and shifts in their voltage dependence contribute to spontaneous firing and heightened pain sensitivity. By identifying a dual mechanism by which cholesterol regulates HCN channels—via both OMD expansion and increased inner-leaflet cholesterol—we provide a framework for understanding how membrane composition alters excitability in disease states. Importantly, our results demonstrate that a decrease in free cholesterol levels at the membrane following nerve injury may not just be correlational but functionally linked to pain behaviors. We demonstrate that cholesterol depletion sensitizes naïve animals to mechanical stimuli, whereas cholesterol supplementation attenuates mechanical hypersensitivity in a neuropathic pain model. These pain-related phenotypes are accompanied by reduced homo-FRET between cholesterol sensors and distinct alterations in HCN channel gating, including shifts in voltage sensitivity and activation kinetics. The ability to temporally separate the effects of OMD expansion from those of cholesterol accumulation using biophysical and imaging tools allowed us to link specific gating changes to defined phases of membrane remodeling. Notably, changes in slope factor (V_s) were more closely associated with OMD expansion, while shifts in half-maximal activation voltage ($V_{1/2}$) and time constants were more sensitive to increased cholesterol content in the inner leaflet.

This dual sensitivity of HCN channels likely stems from their unique structural features. The long S4 voltage-sensing helix in HCN channels, which spans a considerable portion of the membrane electric field, is particularly responsive to changes in membrane order and lipid packing (27, 35, 36). Furthermore, the presence of putative cholesterol-binding motifs in HCN channel subtypes raises the possibility of direct cholesterol-channel interactions that modulate gating. In addition, cholesterols could regulate other membrane lipids and indirectly modulate channel activities (44-47), which remains an area of future investigation. These features make HCN channels highly susceptible to lipid-mediated modulation,

offering a mechanistic explanation for their dynamic behavior in sensory neurons under inflammation or injury. From a translational perspective, these findings raise the possibility that manipulating membrane cholesterol—either pharmacologically or genetically—could serve as a strategy for tuning HCN channel function and alleviating chronic pain. While current therapies targeting HCN channels have largely focused on pharmacological pore-blockers, our work suggests that modulating the HCN voltage sensor/OMD interactions or the lipid environment itself could achieve similar outcomes.

In summary, this study provides new insights into the biophysical mechanisms by which cholesterol and OMDs regulate ion channel activity, with relevance for HCN channel function in nociceptors. By bridging molecular imaging, electrophysiology, and in vivo behavior, we present a view of how membrane lipid remodeling contributes to neuronal hyperexcitability and pain. This integrative framework offers new insights for understanding and treating neuropathic pain by targeting the membrane environment.

MATERIALS AND METHODS

Cell Culture and Molecular Reagents

The tsA-201 cell line, a variant of human embryonic kidney (HEK293) cells, was sourced from Sigma-Aldrich (St. Louis, MO). These cells were maintained in Dulbecco's modified Eagle's medium (DMEM; Gibco) supplemented with 10% fetal bovine serum (FBS; Gibco) and 1% penicillin/streptomycin (Gibco) under humidified conditions at 37°C with 5% CO_2 in tissue culture dishes (CellTreat, Pepperell, MA). Transfection of tsA-201 cells at 70%-90% confluency was performed using the Lipofectamine 3000 Kit (Invitrogen, Carlsbad, CA, #L30000080) following established protocols.

Cholera toxin subunit B (CTxB) conjugated to Alexa Fluor™ 488 and 647 was obtained from Thermo Fisher Scientific and applied to cultured cells at a concentration of 20 nM for approximately 10 minutes. CTxB binds to GM1-enriched membranes with a picomolar affinity. β-Cyclodextrin, α-cyclodextrin and water-soluble cholesterol were purchased from Sigma-Aldrich (St. Louis, MO). The eGFP-GRAM-W plasmid was obtained from Addgene (#211701). The C-terminal mCherry tagged OlyA was synthesized and purified by GenScript (Piscataway, NJ), and was applied to cultured cells at a concentration of 1 uM for ~1 hour. Before imaging, OlyA-treated cells were incubated in regular DMEM medium for 30 mins to wash away unbound OlyA.

FLIM-FRET and Fluorescence Anisotropy

Fluorescence microscopy and FLIM experiments was performed like previous research (8). A laser scanning confocal system with a FastFLIM data acquisition module (ISS, Inc.) and two hybrid PMT detectors (Hamamatsu) was used for frequency-domain FLIM imaging. A supercontinuum laser (YSL Photonics) provided excitation at specific wavelengths for CFP, GFP, AF-488, and mCherry with consistent laser intensity across samples. Emission was detected using dichroic cubes and filters optimized for CFP/YFP and AF-488/AF-555 FRET pairs. Confocal images (256 × 256 pixels) were acquired using a 100 μm pinhole and pixel dwell times of 0.1 ms, with signal accumulated over three repeats. Image acquisition and processing were performed with VistaVision software (ISS, Inc.), enabling phasor plotting and FLIM analysis (8, 48-50). A smoothing filter and intensity-threshold filter were applied to isolate membrane-localized lifetime signals. The phasor FLIM approach distinguished membrane fluorescence from cytosolic and background signals, allowing separation of endocytosed and membrane-localized CTxB. Phase delays (φ) and modulation ratios (m) were determined using Fourier transforms, accounting for the instrument response function calibrated with fluorophores of known lifetimes (Atto 425,

rhodamine 110, rhodamine B) (49). FLIM-FRET analysis was conducted with the VistaVision FRET trajectory function, optimizing background and donor contributions for accuracy, maintaining background levels below 5% to minimize interference.

Fluorescence anisotropy was used to assess the membrane localization and dynamics of eGFP-GRAM-W and mCherry-tagged OlyA proteins. Anisotropy measurements were performed using a polarization module integrated with a confocal microscope, enabling simultaneous acquisition. The system included a halfwave plate and a linear polarizer assembly at the laser entrance, both of which were rotatable with 1-degree precision over 360 degrees to define the excitation polarization state. Emission fluorescence was separated into parallel ($I_{\parallel}$) and perpendicular ($I_{\perp}$) components relative to the excitation polarization using a polarization beam splitter assembly, allowing for precise anisotropy measurements. Cells labeled with membrane-localized GFP- or mCherry-tagged constructs were cultured on glass-bottom dishes and maintained in imaging buffer to preserve physiological conditions. Anisotropy was determined using a software package in VistaVision that acquired fluorescence intensity in the two detection channels, with background subtraction applied to correct for autofluorescence and cytosolic fluorescence. The fluorescence anisotropy (r) at the plasma membrane was calculated using the equation: $r = (I_{\parallel} - I_{\perp}) / (_{\parallel} + 2*I_{\perp})$ (31, 51).

The homo-FRET efficiency of GRAM-W was estimated using fluorescence anisotropy measurements at the plasma membrane and in the cytoplasmic region following β-cyclodextrin treatment. After 5 minutes of cholesterol extraction with β-cyclodextrin, GRAM-W exhibited near-complete translocation to the cytosol, where the measured anisotropy of 0.375 was assumed to represent a state minimally affected by homo-FRET and was designated as r'. This assumption is based on the typical cytosolic concentration of constructs following overexpression, which ranges from 1-10 μM, corresponding to average intermolecular distances of approximately 118 nm (for 1 μM) to 55 nm (for 10 μM) in a 3-D space. Given that the Förster distance (R_0) for homo-FRET between GFP molecules is approximately 5 nm, these large intermolecular distances in the cytosol are expected to preclude significant homo-FRET interactions. The homo-FRET efficiency was then calculated using the equation $E_{homo\text{-}FRET} = 1 - r/r'$, where r is the measured anisotropy at the plasma membrane and r' is the cytosolic anisotropy (0.375), serving as the reference value in the absence of homo-FRET (31, 52). The homo-FRET efficiency of OlyA-mCherry was estimated using a similar approach. The anisotropy of OlyA-mCherry in the absence of homo-FRET was measured to be 0.251 using purified OlyA-mCherry dissolved (5 μM) in dPBS.

Rat Studies and Primary Dorsal Root Ganglion (DRG) Neurons

Pathogen-free adult Sprague-Dawley rats (females ~100 g, males ~250 g; Envigo, Placentia, CA) were maintained in a controlled environment with a 12-hour light/dark cycle (lights on at 07:00 h) and a regulated temperature of 23 ± 3°C. Food and water were provided ad libitum. All experimental procedures were conducted in accordance with National Institutes of Health guidelines and were approved by the Institutional Animal Care and Use Committee (IACUC) of Saint Louis University. Behavioral testing was performed by researchers blinded to experimental conditions.

Dorsal root ganglia (DRG) from the ipsilateral side of nerve injuries were isolated from 100 g female Sprague-Dawley rats. The dissection involved removing dorsal skin and muscle layers, followed by precise cutting of the vertebral bone processes to expose the DRGs. The excised DRGs were trimmed at their roots and enzymatically digested in 3 mL sterile, bicarbonate-free, serum-free DMEM (Catalog# 11965, Thermo Fisher Scientific, Waltham, MA) supplemented with neutral protease (3.125 mg/mL, Catalog# LS02104, Worthington, Lakewood, NJ) and collagenase Type I (5 mg/mL, Catalog# LS004194, Worthington, Lakewood, NJ). The tissue was incubated for 45 minutes at 37°C with gentle agitation. After digestion, the dissociated DRG neurons (~1.5 × 10^6 cells) were collected by centrifugation, washed with DRG culture medium (DMEM supplemented with 1% penicillin/streptomycin sulfate from a 10,000 µg/mL stock, 30 ng/mL nerve growth factor, and 10% fetal bovine serum), and plated onto 12-mm coverslips coated with poly-D-lysine and laminin.

Spared nerve injury (SNI) Surgery and Von Frey test

Animals were anesthetized with isoflurane (5%) and placed on a heated blanket to preserve body temperature. Anesthesia was maintained (2.5%) throughout the surgery. Areflexia was confirmed before starting the surgery. Chlorhexidine was applied twice on the right leg, and a small incision (2-3 cm) was performed on the thigh. The biceps femoris muscle was bluntly dissected to expose the three terminal branches of the sciatic nerve. The common peroneal and tibial branches were tightly ligated with 4–0 silk and axotomized, leaving the sural branch intact. The muscle was sutured with 5–0 absorbable suture and skin was auto clipped. Antibiotic ointment was applied on the skin. Animals were allowed to recover for 7 days before any testing.

Mechanical allodynia was measured by assessing the withdrawal threshold of the paw in response to probing with a series of calibrated fine (von Frey) filaments. Animals were placed in Plexiglas boxes on an elevated mesh screen and were given 15 minutes to acclimate. Filaments were applied on

the plantar surface of both hind-paws in ascending forces until a withdrawal reflex or until the cut-off filament of 15g. The withdrawal threshold was determined by sequentially increasing and decreasing the stimulus strength (the “up and down” method), and data were analyzed with the nonparametric method of Dixon (53) and expressed as the mean withdrawal threshold.

Patch-Clamp Electrophysiology

Whole-cell patch-clamp recordings were conducted using an EPC10 amplifier in conjunction with PATCHMASTER software (HEKA), employing a 5 kHz sampling rate. Borosilicate glass pipettes were fabricated with a P1000 micropipette puller (Sutter Instrument, Novato, CA), yielding an initial resistance of 2.5–4 MΩ. A Sutter MP-225A motorized micromanipulator was utilized for precise electrode positioning. Experiments were carried out at room temperature.

To measure HCN currents in DRG neurons, the internal pipette solution was composed of (in mM): 10 NaCl, 137 KCl, 4 Mg-ATP, 10 HEPES, 1 EGTA, and adjusted to pH 7.3 with KOH. The 4 mM Mg-ATP is sufficient to prevent $PI(4,5)P_2$ hydrolysis during the whole-cell patch-clamp experiments (54, 55). The extracellular solution consisted of (in mM): 154 NaCl, 5.6 KCl, 1 MgCl2, 1 CaCl2, 8 HEPES, and 10 D-glucose, with pH set to 7.4 using NaOH. Series resistance was consistently maintained below 10 MΩ, with compensation adjusted between 40% and 70%. The conductance-voltage (G-V) relationship of endogenous HCN currents was derived from instantaneous tail currents measured at -60 mV following test pulses ranging from -40 mV to between 0 and -140 mV. Leak-subtracted tail currents at -60 mV were normalized to the maximum tail current amplitude to determine relative conductance (G/G_{max}). These values were plotted as a function of the test pulse voltage and fitted to the Boltzmann equation: $G/G_{max} = 1/(1 + \exp[(V - V_{1/2})/V_S])$, where V represents membrane potential, $V_{1/2}$ denotes the voltage for half-maximal activation, and Vs is the slope factor. The slope factor was defined as $Vs = RT/zeF$, where R is the gas constant, T is the absolute temperature (297 K), F is the Faraday constant, *e* is the elementary charge, and z represents the estimated gating charge per channel required for activation.

For whole-cell sodium channel recordings, we used a reduced extracellular sodium concentration, as established in previous studies, to decrease the electrochemical driving force and enable more effective voltage clamping of fast sodium currents (56). The extracellular solution consisted of (in mM): 35 NaCl, 65 Choline-Cl, 30 TEA (tetraethylammonium)-Cl, 0.1 $CaCl_2$, 5 $MgCl_2$, 0.1 $CdCl_2$, 10 HEPES, and 10 glucose, pH was adjusted to 7.4. The internal pipette solution contained (in mM): 100 Cs-MeS (cesium methanesulfonate), 40 TEA-Cl, 5 NaCl, 1 $CaCl_2$, 11 EGTA, 10 HEPES, 2 Mg-ATP, and 1 GTP, pH was adjusted to 7.4. A p/−4 leak subtraction method was used to cancel passive capacitive transients.

The peak current amplitude at each voltage step was used to construct the G-V relationship for channel activation, after correcting for the voltage-dependent driving force. To estimate the driving force at each membrane potential, we determined the reversal potential by linearly extrapolating peak current amplitudes recorded at depolarized voltages to the voltage at which the net current was zero. Steady-state inactivation was assessed using a voltage protocol consisting of pre-pulse steps from –70 mV to 0 mV, followed by a main test pulse at 0 mV. Peak current amplitudes during the main pulse were normalized to the maximal response and used to estimate post-inactivation conductance.

Statistics and Reproducibility

Data parameters are expressed as mean ± s.e.m. from independent cells or patches. For single-cell imaging or patch-clamp experiments, statistical significance was assessed using paired t-test for comparisons between before and after treatments. For behavior experiments, two-way ANOVA or Mann-Whitney tests were used. Statistical thresholds were set at $*p < 0.05$ and $**p < 0.01$, respectively.

ACKNOWLEDGEMENTS

This research is supported by National Institute of General Medical Sciences R35GM154778 grant (to G.D.), and by the Doisy Fund (to G.D. and L.J.H.) of the Edward A. Doisy Department of Biochemistry and Molecular Biology at Saint Louis University School of Medicine. The Moutal lab is supported by startup funds from the Department of Pharmacology and Physiology, Saint Louis University, SLU Institute for Drug & Biotherapeutic Innovation seed grant, National Institute of Neurological Disorders and Stroke R01NS119263 grant, and Department of Defense CPMRP #CP220080P1 grant. Cartoons in figures were created using BioRender.

AUTHOR CONTRIBUTIONS

G.D. conceptualized the research and designed experiments. L. J. H. performed electrophysiology experiments, G.D. performed fluorescence imaging. C.G., N.L.A.D., L.S., and A.M. performed and analyzed behavior experiments on rats and prepared neuronal samples. G.D., and L. J. H. analyzed data and created figures. G.D. and A.M. wrote the paper.

COMPETING INTERESTS

The authors declare no competing interests.

REFERENCES

1. I. Levitan, D. K. Singh, A. Rosenhouse-Dantsker, Cholesterol binding to ion channels. *Front Physiol* **5**, 65 (2014).
2. K. M. Beverley, I. Levitan, Cholesterol regulation of mechanosensitive ion channels. *Front Cell Dev Biol* **12**, 1352259 (2024).
3. O. Furst, N. D'Avanzo, Isoform dependent regulation of human HCN channels by cholesterol. *Sci Rep* **5**, 14270 (2015).
4. S. L. Veatch, S. L. Keller, Organization in lipid membranes containing cholesterol. *Phys Rev Lett* **89**, 268101 (2002).
5. D. Lingwood, K. Simons, Lipid rafts as a membrane-organizing principle. *Science* **327**, 46-50 (2010).
6. I. Levental, E. Lyman, Regulation of membrane protein structure and function by their lipid nano-environment. *Nat Rev Mol Cell Biol* **24**, 107-122 (2023).
7. D. W. Hilgemann *et al.*, Lipid signaling to membrane proteins: From second messengers to membrane domains and adapter-free endocytosis. *J Gen Physiol* **150**, 211-224 (2018).
8. L. J. Handlin *et al.*, Membrane lipid nanodomains modulate HCN pacemaker channels in nociceptor DRG neurons. *Nat Commun* **15**, 9898 (2024).
9. E. C. Emery, G. T. Young, E. M. Berrocoso, L. Chen, P. A. McNaughton, HCN2 ion channels play a central role in inflammatory and neuropathic pain. *Science* **333**, 1462-1466 (2011).
10. E. C. Emery, G. T. Young, P. A. McNaughton, HCN2 ion channels: an emerging role as the pacemakers of pain. *Trends Pharmacol Sci* **33**, 456-463 (2012).
11. S. Lainez, C. Tsantoulas, M. Biel, P. A. McNaughton, HCN3 ion channels: roles in sensory neuronal excitability and pain. *J Physiol* **597**, 4661-4675 (2019).
12. D. DiFrancesco, Characterization of single pacemaker channels in cardiac sino-atrial node cells. *Nature* **324**, 470-473 (1986).
13. A. Saponaro *et al.*, Gating movements and ion permeation in HCN4 pacemaker channels. *Mol Cell* **81**, 2929-2943 e2926 (2021).
14. W. N. Zagotta *et al.*, Structural basis for modulation and agonist specificity of HCN pacemaker channels. *Nature* **425**, 200-205 (2003).
15. K. B. Craven, W. N. Zagotta, CNG and HCN channels: two peas, one pod. *Annu Rev Physiol* **68**, 375-401 (2006).
16. S. R. Chaplan *et al.*, Neuronal hyperpolarization-activated pacemaker channels drive neuropathic pain. *J Neurosci* **23**, 1169-1178 (2003).
17. G. T. Young, E. C. Emery, E. R. Mooney, C. Tsantoulas, P. A. McNaughton, Inflammatory and neuropathic pain are rapidly suppressed by peripheral block of hyperpolarisation-activated cyclic nucleotide-gated ion channels. *Pain* **155**, 1708-1719 (2014).
18. A. Barbuti *et al.*, Localization of pacemaker channels in lipid rafts regulates channel kinetics. *Circ Res* **94**, 1325-1331 (2004).
19. D. H. Z. Koh *et al.*, Visualization of accessible cholesterol using a GRAM domain-based biosensor. *Nat Commun* **14**, 6773 (2023).
20. B. Ercan, T. Naito, D. H. Z. Koh, D. Dharmawan, Y. Saheki, Molecular basis of accessible plasma membrane cholesterol recognition by the GRAM domain of GRAMD1b. *EMBO J* **40**, e106524 (2021).
21. T. Naito *et al.*, Movement of accessible plasma membrane cholesterol by the GRAMD1 lipid transfer protein complex. *Elife* **8** (2019).
22. S. Endapally *et al.*, Molecular Discrimination between Two Conformations of Sphingomyelin in Plasma Membranes. *Cell* **176**, 1040-1053 e1017 (2019).
23. M. Skocaj *et al.*, Tracking cholesterol/sphingomyelin-rich membrane domains with the ostreolysin A-mCherry protein. *PLoS One* **9**, e92783 (2014).

24. A. Das, M. S. Brown, D. D. Anderson, J. L. Goldstein, A. Radhakrishnan, Three pools of plasma membrane cholesterol and their relation to cholesterol homeostasis. *Elife* **3** (2014).
25. R. Sachl *et al.*, On multivalent receptor activity of GM1 in cholesterol containing membranes. *Biochim Biophys Acta* **1853**, 850-857 (2015).
26. J. Myeong, C. G. Park, B. C. Suh, B. Hille, Compartmentalization of phosphatidylinositol 4,5-bisphosphate metabolism into plasma membrane liquid-ordered/raft domains. *Proc Natl Acad Sci U S A* **118** (2021).
27. L. J. Handlin, G. Dai, Direct regulation of the voltage sensor of HCN channels by membrane lipid compartmentalization. *Nat Commun* **14**, 6595 (2023).
28. G. Dai, Neuronal KCNQ2/3 channels are recruited to lipid raft microdomains by palmitoylation of BACE1. *J Gen Physiol* **154** (2022).
29. I. Decosterd, C. J. Woolf, Spared nerve injury: an animal model of persistent peripheral neuropathic pain. *Pain* **87**, 149-158 (2000).
30. A. N. Bader *et al.*, Homo-FRET imaging as a tool to quantify protein and lipid clustering. *Chemphyschem* **12**, 475-483 (2011).
31. A. Joshi *et al.*, Intermolecular energy migration via homoFRET captures the modulation in the material property of phase-separated biomolecular condensates. *Nat Commun* **15**, 9215 (2024).
32. S. Mahammad, I. Parmryd, Cholesterol depletion using methyl-b-cyclodextrin. *Methods Mol Biol* **1232**, 91-102 (2015).
33. A. E. Christian, M. P. Haynes, M. C. Phillips, G. H. Rothblat, Use of cyclodextrins for manipulating cellular cholesterol content. *J Lipid Res* **38**, 2264-2272 (1997).
34. B. Yu *et al.*, Cryo-EM structure of human HCN3 channel and its regulation by cAMP. *J Biol Chem* **300**, 107288 (2024).
35. C. H. Lee, R. MacKinnon, Structures of the Human HCN1 Hyperpolarization-Activated Channel. *Cell* **168**, 111-120 e111 (2017).
36. C. H. Lee, R. MacKinnon, Voltage Sensor Movements during Hyperpolarization in the HCN Channel. *Cell* **179**, 1582-1589 e1587 (2019).
37. M. Alsaloum *et al.*, Voltage-gated sodium channels in excitable cells as drug targets. *Nat Rev Drug Discov* 10.1038/s41573-024-01108-x (2025).
38. W. A. Catterall, Structure and function of voltage-gated sodium channels at atomic resolution. *Exp Physiol* **99**, 35-51 (2014).
39. S. Albani *et al.*, Depletion of membrane cholesterol modifies structure, dynamic and activation of Na(v)1.7. *Int J Biol Macromol* **278**, 134219 (2024).
40. M. Amsalem, C. Poilbout, G. Ferracci, P. Delmas, F. Padilla, Membrane cholesterol depletion as a trigger of Nav1.9 channel-mediated inflammatory pain. *EMBO J* **37** (2018).
41. G. Wisedchaisri *et al.*, Resting-State Structure and Gating Mechanism of a Voltage-Gated Sodium Channel. *Cell* 10.1016/j.cell.2019.06.031 (2019).
42. I. Decosterd, C. J. Woolf, Spared nerve injury: an animal model of persistent peripheral neuropathic pain. *Pain* **87**, 149-158 (2000).
43. A. Moutal *et al.*, CRISPR/Cas9 editing of Nf1 gene identifies CRMP2 as a therapeutic target in neurofibromatosis type 1-related pain that is reversed by (S)-Lacosamide. *Pain* **158**, 2301-2319 (2017).
44. D. O. Kwarteng *et al.*, Cholesterol affects the binding of proteins to phosphatidic acid without influencing its ionization properties. *J Lipid Res* **66**, 100749 (2025).
45. M. Delgado-Ramirez, A. L. Lopez-Serrano, S. Sanchez-Armass, U. Meza, A. A. Rodriguez-Menchaca, Crosstalk between cholesterol and PIP_2 in the regulation of Kv7.2/Kv7.3 channels. *Biol Chem* **405**, 161-165 (2024).
46. D. M. Taglieri, D. A. Delfin, M. M. Monasky, Cholesterol regulation of PIP(2): why cell type is so important. *Front Physiol* **3**, 492 (2012).

47. L. J. Pike, J. M. Miller, Cholesterol depletion delocalizes phosphatidylinositol bisphosphate and inhibits hormone-stimulated phosphatidylinositol turnover. *J Biol Chem* **273**, 22298-22304 (1998).
48. M. A. Digman, V. R. Caiolfa, M. Zamai, E. Gratton, The phasor approach to fluorescence lifetime imaging analysis. *Biophys J* **94**, L14-16 (2008).
49. L. Malacrida, S. Ranjit, D. M. Jameson, E. Gratton, The Phasor Plot: A Universal Circle to Advance Fluorescence Lifetime Analysis and Interpretation. *Annu Rev Biophys* **50**, 575-593 (2021).
50. S. Ranjit, L. Malacrida, D. M. Jameson, E. Gratton, Fit-free analysis of fluorescence lifetime imaging data using the phasor approach. *Nat Protoc* **13**, 1979-2004 (2018).
51. G. Dai, Z. M. James, W. N. Zagotta, Dynamic rearrangement of the intrinsic ligand regulates KCNH potassium channels. *J Gen Physiol* **150**, 625-635 (2018).
52. T. S. van Zanten, G. P. S, S. Mayor, Quantitative fluorescence emission anisotropy microscopy for implementing homo-fluorescence resonance energy transfer measurements in living cells. *Mol Biol Cell* **34**, tp1 (2023).
53. S. R. Chaplan, F. W. Bach, J. W. Pogrel, J. M. Chung, T. L. Yaksh, Quantitative assessment of tactile allodynia in the rat paw. *J Neurosci Methods* **53**, 55-63 (1994).
54. G. Dai, H. Yu, M. Kruse, A. Traynor-Kaplan, B. Hille, Osmoregulatory inositol transporter SMIT1 modulates electrical activity by adjusting PI(4,5)P_2 levels. *Proc Natl Acad Sci U S A* **113**, E3290-3299 (2016).
55. P. Pian, A. Bucchi, A. Decostanzo, R. B. Robinson, S. A. Siegelbaum, Modulation of cyclic nucleotide-regulated HCN channels by PIP_2 and receptors coupled to phospholipase C. *Pflugers Arch* **455**, 125-145 (2007).
56. X. Zhang, B. T. Priest, I. Belfer, M. S. Gold, Voltage-gated Na^+ currents in human dorsal root ganglion neurons. *Elife* **6** (2017).